

**Impact of long and short-range atomic ordering on
ferroelectric properties of perovskite-based lead-free
functional materials**



**Thesis submitted in partial fulfillment
for the Award of
DOCTOR OF PHILOSOPHY
in
PHYSICS**

by
DIGVIJAY NATH DUBEY

Under the supervision of
Dr. Saurabh Tripathi

**DEPARTMENT OF PHYSICS
INDIAN INSTITUTE OF TECHNOLOGY
BANARAS HINDU UNIVERSITY
VARANASI - 221 005**

ROLL NUMBER
17171006

YEAR OF SUBMISSION
2022

I would like to dedicate this thesis to my loving parents and amazing friends, whose support and motivation kept me going through the tough times.

Certificate

It is certified that the work contained in the thesis titled **“Impact of long and short-range atomic ordering on ferroelectric properties of perovskite-based lead-free functional materials”** by **Mr. Digvijay Nath Dubey**, Roll Number **17171006**, has been carried out under my supervision and that this work has not been submitted elsewhere for a degree.

Signature:

S. Tripathi

Supervisor

Dr. Saurabh Tripathi

(Assistant Professor)

Department of Physics

Indian Institute of Technology (BHU),

Varanasi-221005 (U.P.), India

Assistant Professor

Department of Physics

Indian Institute of Technology

(Banaras Hindu University)

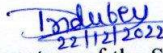
Varanasi-221005

Declaration

I, **Digvijay Nath Dubey**, certify that the work embodied in this thesis is my own bona-fide work and carried out by me under the supervision of **Dr. Saurabh Tripathi** from July 2017 to December 2022 at the **Department of Physics**, Indian Institute of Technology (BHU), Varanasi. The matter embodied in this thesis has not been submitted for the award of any other degree/diploma. I declare that I have faithfully acknowledged and given credits to the research workers whenever and wherever their works have been cited in my work in this thesis. I further declare that I have not wilfully copied any others' work, paragraphs, text, data, results, etc., reported in journals, books, magazines, reports dissertations, theses, etc., or available at websites and have not included them in this thesis and have not cited as my own work.

Date: 22/12/2022


Place: IIT (BHU), Varanasi



Signature of the Student

(Digvijay Nath Dubey)

Certificate by the Supervisor

It is certified that the above statement made by the student is correct to the best of my knowledge.

Signature: 
Supervisor
(Dr. Saurabh Tripathi)
Assistant Professor
Department of Physics
Indian Institute of Technology,
(Banaras Hindu University)
Varanasi-221005


Signature of the Head of the Department
(Prof. Sandip Chatterjee)
HEAD/विभागाध्यक्ष
भौतिकी विभाग/Deptt. of Physics
भा०प्रौ०सं०/(का०हि०वि०)/IIT (BHU)
वाराणसी/Varanasi-221005

Copyright Transfer Certificate

Title of the Thesis : Impact of long and short-range atomic ordering on ferroelectric properties of perovskite-based lead-free functional materials


Name of the Student : Digvijay Nath Dubey

Copyright Transfer

The undersigned hereby assigns to the Indian Institute of Technology (Banaras Hindu University) Varanasi all rights under copyright that may exist in and for the above thesis submitted for the award of the **Doctor of Philosophy in Physics**.

Date: 22/12/2022

Place: IIT (BHU), Varanasi


Signature of the Student

(Digvijay Nath Dubey)

Note: However, the author may reproduce or authorize others to reproduce material extracted verbatim from the thesis or derivative of the thesis for author's personal use provided that the source and the Institute's copyright notice are indicated.

Acknowledgements

There are number of people I would like to acknowledge who supported me in different ways throughout this challenging but enjoyable academic journey of Ph.D.

First of all, I would like to thank my supervisor, Dr. Saurabh Tripathi, for all of his consistent guidance and incredible encouragement provided by him, while working with me over the past five years. In addition, I thank my RPEC members, Prof. Sandip Chatterjee and Dr. Akhilesh Kumar Singh, for the comments provided by him regarding my research work. I will also like to thank all faculty members, and the non-teaching staff of the Department of Physics, IIT (BHU) for their supports in a direct or indirect way.

I would like to express my thanks to our collaborators Dr. Gurvinderjit Singh (RRCAT, Indore), Dr. Rahul Shukla (RRCAT, Indore), Dr. Akhilesh Kumar Singh (IIT BHU), Dr. S K. Mishra (BARC, MUMBAI), Dr. Abhishek Pandey (Univ. of Witwatersrand), Dr. Rudolph Erasmus (Univ. of Witwatersrand) for their help in carrying out different measurements and characterizations as per our requirements.

I would like to extend my thanks to my friend Abhishek, Rohit, Prashant Pandey, Vivek, Vaibhav, Alam, Prashant Dixit, Balveer, Rajkumar, Pankaj, Manish, Deepak for making this journey enjoyable despite several ups and downs. In addition, I express my thanks to fellow philosophers Anuvrat, Harsh, and Abhinav for the fruitful discussions related to the research work.

I would like to express special thanks to my amazing parents and other family members. However, no words can sum up the gratitude that I have for my parents and family members for their consistent support throughout this academic journey.

Finally, I will always be grateful to Almighty God for endless grace.

Digvijay Nath Dubey

Abstract

Perovskites (ABO_3) are the class of materials where slight distortion in the crystallographic structure leads to a drastic change in the physical properties such as ferroelectricity, ferromagnetism, ferroelasticity, etc. Out of these, ferroelectrics are the materials that exhibit diverse functionality and find enormous applications in sensors, actuators, transducers, energy harvesters, memory devices, etc. Nowadays, the field of nearly all these applications is dominated by lead-based ceramic systems. However, the adverse environmental concerns associated with the lead-based ferroelectric materials imposed by their toxic nature have intensified the search for lead-free alternatives. In this regard, 'A' and 'B' site-modified perovskite barium titanate ($BaTiO_3$)-based solid solutions have emerged as highly appealing technologically important lead-free candidates due to their potential to exhibit various tunable crystallographic structural phase transitions leading to different phase boundaries, and the relaxor ferroelectric behaviour. The term phase boundary comprises the polymorphic and morphotropic phase boundaries, where the free energy barrier between the coexisting phases (long-range ordered) gets reduced, facilitating the easy polarization rotation phenomenon to realize the high electromechanical responses. The polarization rotation phenomenon occurs when the phase transitions are ferroelectric-ferroelectric in nature and corresponds to different directions of polarization. These ferroelectric phases are described by the freezing of zone center (Γ_4^-) phonon mode belonging to the high symmetry cubic phase, whose amplitude determines the magnitude of the intrinsic contribution in the ferroelectricity present in the material. On the other hand, the fascinating properties of relaxor ferroelectrics are driven by the exotic polar nano-regions (short-range ordered) existing in the average cubic phase. The main characteristic feature of the relaxor is the existence of a broad phase transition temperature which is often beneficial since it leads to an increase in the thermal stability of the physical responses of the system and hence makes

the materials operational over a wide range of temperatures. Thus, the physical properties are highly sensitive to the crystallographic phases of the materials, and the macroscopic (long-range) as well as microscopic (short-range) atomic ordering plays a crucial role in predicting the suitability of the material for various application purposes.

Thus owing to the idea of relaxor ferroelectrics driven by short-range ordering (polar nano-regions), first, we have developed a lead-free perovskite-based solid solution $(\text{Ba}_{1-x}\text{Ca}_x)(\text{Sn}_{0.11}\text{Zr}_{0.05}\text{Ti}_{0.84})\text{O}_3$; BCSZTx ($0 \leq x \leq 0.20$), exhibiting relaxor ferroelectric behaviour in an average cubic structure. X-ray diffraction measurements for all the compositions have shown a simple cubic phase with $Pm\bar{3}m$ space group. Despite having a centrosymmetric cubic phase, a slim hysteresis loop has been observed via PE loop measurements. This contrapositive behaviour was explained via Raman spectroscopic measurements which reveals the presence of local ordering in the macroscopic cubic matrix, corresponding to the 'A' and 'B' sites. The cooperative behaviour of 'A' and 'B' site off-centered (local) atoms leading to microscopic polar symmetry in the macroscopically cubic matrix is held responsible for the relaxor ferroelectric nature of BCSZTx ceramics. Owing to the aforementioned contrapositive behaviour, BCSZTx ceramics exhibit a high value of dielectric constant. Eventually, we have observed a decisive role of Ca^{2+} dopant at the 'A' site in BCSZTx system leading to the enhancement in the relaxor ferroelectric behaviour and hence dielectric properties. The presence of a slim hysteresis loop, along with broad and diffuse dielectric nature, makes these ceramics a potential candidate for energy storage applications.

Further, in order to explore the evolution of crystallographic phases as a function of temperature for relaxor ferroelectric system BCSZTx, we have carried out temperature-dependent X-ray diffraction and Raman spectroscopic studies for one of the important compositions, viz., BCSZT15. The Rietveld refinements performed on temperature-dependent X-ray diffraction data revealed a single cubic ($Pm\bar{3}m$) phase for $248 \text{ K} \leq T \leq 448 \text{ K}$,

while the coexistence of the disordered cubic ($Pm\bar{3}m$) phase with the ordered rhombohedral ($R3m$) phase for $100 \text{ K} \leq T \leq 223 \text{ K}$. The results of temperature-dependent X-ray diffraction analysis in conjunction with Raman spectroscopic studies reveals the overall crystallographic structure of BCSZTx ceramics. Further, the evolution of lattice parameter, and unit cell volume corresponding to the cubic ($Pm\bar{3}m$) phase show a saturation as a function of temperature, revealing the presence of an electrostrictive-like effect in the material, making the composition suitable for actuators.

Subsequently, in order to study the role of inter-ferroelectric phase boundary, *i.e.*, the coexistence of ferroelectric phases (with long-range atomic arrangements), driven by component freezing of three-dimensional polar (Γ_4^-) phonon mode corresponding to the center of cubic Brillouin zone, we have fabricated another scientifically enriched and technologically important BaTiO₃-based eco-friendly functional material $(\text{Ba}_{0.92}\text{Ca}_{0.08})(\text{Zr}_{0.05}\text{Ti}_{0.95-x}\text{Sn}_x)\text{O}_3$; BCZTSn_x ($0 \leq x \leq 0.10$) via solid-state reaction method. The combined X-ray diffraction, Raman spectroscopic analysis, and temperature-dependent dielectric studies have revealed the presence of several crystallographic phase transitions with coexisting phases, *viz.*, $P4mm \rightarrow (P4mm + Amm2 + R3m) \rightarrow (Amm2 + R3m) \rightarrow R3m \rightarrow (Pm\bar{3}m + R3m)$, as a function of Sn(*x*) content. These crystallographic phases, *viz.*, $P4mm$, $Amm2$, and $R3m$ results due to component(s) freezing of Γ_4^- phonon mode (belonging to $Pm\bar{3}m$ space group), with order parameter directions (0,0,a), (a,a,0), and (a,a,a) leading to ferroelectric polarization along $\langle 001 \rangle$, $\langle 110 \rangle$, and $\langle 111 \rangle$ directions, respectively. The BCZTSn_x ceramic system corresponding to Sn(*x*) = 0.025 exhibits a significant reduction in the coercive field (E_c) with an enhancement in ferroelectric polarization (P_r) in comparison to the composition having Sn(*x*) = 0. The enhancement in ferroelectric polarization for Sn(*x*) = 0.025 has been attributed to the inter-ferroelectric three-phase ($P4mm + Amm2 + R3m$) coexistence, which is further explained by the enhancement in the amplitudes of ferroelectric phonon modes (calculated using the symmetry mode analysis technique) corresponding to orthorhombic

and rhombohedral phases. The existence of a high ferroelectric polarization and low coercive field makes the above composition ($\text{Sn}(x) = 0.025$) an eco-friendly candidate for various ferroelectric devices.

Finally, we have extended our studies and synthesized the solid solutions having higher Sn content, *i.e.*, BCZTSn_x ($0.125 \leq x \leq 0.25$). The X-ray diffraction studies inferred a long-range cubic phase with $Pm\bar{3}m$ space group for all the compositions. However, Raman spectroscopic studies have revealed the presence of rhombohedral-like short-range ordering in contrast to the cubic phase inferred from X-ray diffraction analysis. Owing to the presence of short-range ordering driven polar nano-regions, the dielectric studies have shown broad peak with a relaxor ferroelectric nature. Further, the dielectric peak broadening and the relaxor nature increases with increase in $\text{Sn}(x)$ content. Like the lead-based relaxors, *e.g.*, $\text{Pb}(\text{Mg}_{1/3}\text{Nb}_{2/3})\text{O}_3$, where the relaxor nature appears due to random electric fields driven by the charge disorder, the relaxor ferroelectricity in BCZTSn_x is attributed to the random stress fields. The random stress field in BCZTSn_x ceramics is attributed to the disordered distribution of Sn^{4+} cations corresponding to 'B' sites, effectively disrupting the long-range correlated O-Ti-O chain leading to a relaxor ferroelectric behaviour.

Thus, overall, the thesis is focused on the role of long-range ordered inter-ferroelectric phase boundaries (driven by freezing of zone center phonon modes associated with the $Pm\bar{3}m$ space group) and short-range atomic ordering in tuning the dielectric and ferroelectric properties of lead-free perovskite-based functional materials suitable for various technological applications.

Table of contents

List of figures	xxi
List of tables	xxvii
Nomenclature	xxviii
1 Introduction and literature review	1
1.1 Motivation of thesis	1
1.2 Ferroelectricity	3
1.2.1 Definition, characteristics, and other related phenomena	4
1.3 Perovskite structure	8
1.3.1 Tolerance factor and structural stability	8
1.3.2 Theories to explain ferroelectricity in perovskites	10
1.3.3 Role of soft phonon modes in structural phase transformation of perovskites	12
1.3.4 Barium titanate: The first ferroelectric perovskite	13
1.4 Idea of phase coexistence in the enhancement of physical properties . . .	16
1.4.1 Morphotropic and polymorphic phase boundary	17
1.5 Relaxor ferroelectrics	21
1.5.1 Definition and characteristics	21
1.5.2 Some models for relaxor ferroelectrics	25

1.6	Literature review on some BaTiO ₃ -based lead-free functional materials . . .	29
1.6.1	(Ba,Ca)TiO ₃	29
1.6.2	Ba(Sn,Ti)O ₃	31
1.6.3	Ba(Zr,Ti)O ₃	35
1.6.4	(Ba,Ca)(Zr,Ti)O ₃	39
1.6.5	(Ba,Ca)(Sn,Ti)O ₃	41
1.7	Organisation of the thesis	43
2	Experimental procedure and characterization techniques	45
2.1	Sample synthesis	45
2.1.1	Solid-state reaction method	46
2.2	Characterization techniques	47
2.2.1	X-ray diffraction method	47
2.2.2	Dielectric measurement	51
2.2.3	Polarization vs. Electric field (PE) hysteresis loop measurements	53
2.2.4	Raman spectroscopic measurements	55
2.2.5	Microstructural measurement	57
3	Effect of calcium (Ca) dopant at ‘A’ site in tuning the ferroelectricity of average cubic ($Pm\bar{3}m$) phase in a perovskite (ABO₃)-based lead-free (Ba_{1-x}Ca_x)(Sn_{0.11}Zr_{0.05}Ti_{0.84})O₃ system	61
3.1	Introduction	61
3.2	Experimental procedure	64
3.3	Results and discussions	64
3.3.1	X-ray diffraction studies	64
3.3.2	Dielectric studies	67
3.3.3	Polarization vs. Electric field (PE) hysteresis loop analysis	72

3.3.4	Raman spectroscopic studies	74
3.4	Conclusion	79
4	Study of temperature-dependent crystallographic phase evolution in relaxor ferroelectric (Ba_{0.85}Ca_{0.15}) (Sn_{0.11}Zr_{0.05}Ti_{0.84})O₃ system	81
4.1	Introduction	81
4.2	Experimental procedure	82
4.3	Result and discussion	83
4.3.1	Temperature-dependent X-ray diffraction analysis	83
4.3.2	Temperature-dependent Raman spectroscopic studies	91
4.4	Conclusion	94
5	Role of ferroelectric soft phonon mode (Γ_4^-) in tuning the inter-ferroelectric phase boundary of lead-free (Ba_{0.92}Ca_{0.08}) (Zr_{0.05}Ti_{0.95-x}Sn_x)O₃; ($0 \leq x \leq 0.10$) system for enhanced ferroelectric polarization	95
5.1	Introduction	95
5.2	Experimental Procedure	97
5.3	Results and discussions	99
5.3.1	Microstructural analysis	99
5.3.2	Dielectric studies	102
5.3.3	Raman spectroscopic analysis	103
5.3.4	X-ray diffraction studies	107
5.3.5	Symmetry mode analysis	118
5.3.6	Polarization vs. Electric field (PE) hysteresis loop analysis	126
5.3.7	Temperature-dependent Raman spectroscopic studies	129
5.4	Conclusion	135

6	Relaxor ferroelectricity driven by microscopically off-centered atoms in the macroscopic cubic phase of lead-free $(\text{Ba}_{0.92}\text{Ca}_{0.08})(\text{Zr}_{0.05}\text{Ti}_{0.95-x}\text{Sn}_x)\text{O}_3$; ($0.125 \leq x \leq 0.25$) system	137
6.1	Introduction	137
6.2	Experimental methods	139
6.3	Results and discussions	140
6.3.1	X-ray diffraction studies	140
6.3.2	Dielectric studies	143
6.3.3	Raman spectroscopic studies	149
6.4	Conclusion	155
7	Summary and future work suggestions	157
7.1	Summary	157
7.2	Future work suggestions	160
	References	161

List of figures

1.1	Polarization vs. electric field (PE) hysteresis loop for a typical ferroelectric, having the remnant polarization (P_r) and coercive field (E_c).	5
1.2	Representation of direct and converse piezoelectric effect.	7
1.3	The representation of the unit cell of an ideal cubic perovskite (ABO_3) structure.	8
1.4	The representation of different points in the Brillouin zone of the cubic lattice.	12
1.5	Temperature-dependent variation in the dielectric permittivity of barium titanate [1].	14
1.6	Schematic representation of off-centered Ti atom along $\langle 111 \rangle$ directions in (a) rhombohedral, (b) orthorhombic, (c) tetragonal, and (d) cubic phases of $BaTiO_3$ [2].	15
1.7	Schematic representation of polymorphic phase boundary (PPB) and morphotropic phase boundary (MPB) existing between two ferroelectric phases, F_1 and F_2	18
1.8	Morphotropic phase boundary in $Pb(Zr,Ti)O_3$ [3].	19
1.9	Schematic representation of polar directions in monoclinic M_A , M_B , and M_C phases [4].	20

1.10	Schematic representation of dielectric permittivity behaviour exhibited by relaxor ferroelectrics [5].	22
1.11	Schematic representation of polar nano-regions in the cubic matrix.	23
1.12	(a) Phase diagram of $\text{BaTiO}_3\text{-}x\text{CaTiO}_3$ ceramics [6], (b) representation of off-centered calcium atoms in the tetragonal phase of $\text{BaTiO}_3\text{-}x\text{CaTiO}_3$ [7], and (c) the relative energies of $\text{BaTiO}_3\text{-}x\text{CaTiO}_3$; $x = 0.125$ for off-centered Ca atoms along [001], [111], and [113] directions [7].	30
1.13	Phase diagram of $\text{Ba}(\text{Sn},\text{Ti})\text{O}_3$ as a function of Sn content [8].	32
1.14	(a) The dipole-dipole interaction in BaTiO_3 (b) and the interaction between the dipoles in $\text{Ba}(\text{Sn}_{0.20}\text{Ti}_{0.80})\text{O}_3$; The blue and green colours represent the Ti and Sn atoms [9].	34
1.15	Phase diagram of $\text{BaTiO}_3\text{-BaZrO}_3$ [6].	36
1.16	Temperature-dependent evolution of polar nano-regions in relaxor ferroelectric state of $(\text{Ba},\text{Zr})\text{TiO}_3$. Blue colour and red colours correspond to the Ti and Zr ions [10].	38
1.17	Phase diagram of $\text{BZT-}x\text{BCT}$ ceramics [11].	39
1.18	Revised phase diagram of $\text{BZT-}x\text{BCT}$ ceramics [12].	40
1.19	Phase diagram of $\text{Ba}(\text{Sn}_{0.12}\text{Ti}_{0.88})\text{O}_3\text{-}x(\text{Ba}_{0.70}\text{Ca}_{0.30})\text{TiO}_3$ ceramics [13].	42
2.1	The instruments used in the synthesis of samples via solid-state reaction method.	46
2.2	Representation of X-ray diffraction by a crystal.	48
2.3	Rigaku SmartLab high-resolution X-ray diffractometer.	49
2.4	Impedance analyser used for dielectric measurements.	53
2.5	Polarization vs. electric field (PE) hysteresis loop tracer.	54
2.6	Renishaw InVia Raman spectrometer.	57
2.7	High-resolution scanning electron microscope.	58

3.1	Evolution of 200, 220, and 222, X-ray diffraction peaks for BCSZTx ($0 \leq x \leq 0.20$) ceramics.	65
3.2	Rietveld refinement plots for X-ray diffraction pattern of BCSZTx ($0 \leq x \leq 0.20$) ceramics using $Pm\bar{3}m$ space group. The observed pattern is represented by open (red) circles, the continuous line (black) represents the simulated patterns, the vertical bars (gray) correspond to Bragg positions, and the continuous lines (blue) below the vertical bars correspond to the difference between observed and simulated patterns.	66
3.3	Temperature-dependent variation of real (ϵ') and imaginary (ϵ'') parts of dielectric constant for BCSZTx ($0 \leq x \leq 0.20$) ceramics at 100 kHz. . . .	68
3.4	Variation of $\frac{\partial \epsilon'(T)}{\partial T}$ for BCSZTx ($0 \leq x \leq 0.20$) ceramics at 100 kHz. . . .	69
3.5	Variation in ΔT_m of BCSZTx ($0 \leq x \leq 0.20$) ceramics.	70
3.6	The room temperature PE loop behaviour of BCSZTx ($0 \leq x \leq 0.20$) ceramics.	72
3.7	Variation of agreement factor (R_{wp}) after providing local displacements to the cations corresponding to 'A' and 'B' sites along [100] and [111] directions, respectively [14].	75
3.8	Room temperature Raman spectra of BCSZTx ($0 \leq x \leq 0.20$) ceramics. .	76
3.9	The peak fitting for the Raman spectra of BCSZTx ($0 \leq x \leq 0.20$) ceramics.	77
3.10	The variation in peak width and position for 512.8 cm^{-1} mode as a function of Ca content.	78
4.1	Temperature-dependent evolution of the peak profile corresponding to 200, 220, and 222 reflections for BCSZT15.	84
4.2	Rietveld fitted temperature-dependent diffraction pattern of BCSZT15 at some selected temperatures.	85

4.3	Variation of lattice parameter, volume of the unit cell, and phase fractions with temperature for BCSZT15.	86
4.4	Temperature-dependent Raman spectra of BCSZT15.	92
5.1	High-resolution scanning electron micrographs of the sintered pellets of BCZTS _n x (0 ≤ x ≤ 0.10) ceramics.	100
5.2	The histograms depicting the grain size distribution in BCZTS _n x (0 ≤ x ≤ 0.10) ceramics.	101
5.3	Variation in real (ϵ') and imaginary (ϵ'') parts of dielectric permittivity as a function of temperature for BCZTS _n x (0 ≤ x ≤ 0.10) ceramics at 143 kHz.	103
5.4	Raman spectra of BCZTS _n x (0 ≤ x ≤ 0.10) ceramics measured at room temperature.	105
5.5	Evolution of 200, 220, and 222 peaks profiles for BCZTS _n x (0 ≤ x ≤ 0.10) ceramics.	108
5.6	Rietveld fitted X-ray diffraction peak profiles for BCZTS _n x (0 ≤ x ≤ 0.10) ceramics. For each panel, the observed pattern is represented by the open (red) circles, the simulated pattern is represented via continuous (black) lines, the vertical lines (gray) correspond to the Bragg reflections, while the continuous horizontal line (blue) below the vertical bars corresponds to the difference between the observed and simulated patterns.	109
5.7	Rietveld fitted X-ray diffraction peak profile evolution corresponding to 200, 220, and 222 reflections for x = 0.025, via (a) <i>P4mm</i> (b) <i>Amm2</i> (c) <i>P4mm</i> + <i>R3m</i> (d) <i>Amm2</i> + <i>R3m</i> (e) <i>P4mm</i> + <i>Amm2</i> , and (f) <i>P4mm</i> + <i>Amm2</i> + <i>R3m</i> models. The arrow mark indicates the peaks that could not be indexed using the particular model.	111

5.8	Rietveld fitted X-ray diffraction peak profile evolution corresponding to 200, 220, and 222 reflections for $x = 0.05$, via (a) $Amm2$ and (b) $Amm2 + R3m$ models. The arrow mark indicates the peak that could not be indexed using the particular model.	115
5.9	Variation of average Ti-O bond length corresponding to cubic ($Pm\bar{3}m$), tetragonal ($P4mm$), orthorhombic ($Amm2$), and rhombohedral ($R3m$) phases for BCZTSnx ($0 \leq x \leq 0.10$) ceramics.	116
5.10	Variation in amplitude of polar (Γ_4^-) and nonpolar (Γ_5^-) phonon mode for BCZTSnx ceramics as a function of Sn(x) content.	124
5.11	Atomic displacements pattern for various ferroelectric phases of $x = 0.025$, driven by component(s) freezing of polar (Γ_4^- ; involved in symmetry breaking to $P4mm$, $Amm2$, and $R3m$ phases), and nonpolar (Γ_5^- ; responsible for antiferroelectric displacements in $Amm2$ phase) zone center ($k = 0,0,0$) phonon modes belonging to the high symmetry cubic ($Pm\bar{3}m$) phase. . . .	125
5.12	Polarization vs. Electric field (PE) hysteresis loops for BCZTSnx ($0 \leq x \leq 0.10$) ceramics measured at room temperature.	127
5.13	Temperature-dependent Raman spectra of $x = 0.025$	131
5.14	Temperature-dependent Raman spectra of $x = 0.05$	132
5.15	Temperature-dependent Raman spectra of $x = 0.075$	133
6.1	The evolution of 200, 220, and 222, X-ray diffraction peak profiles for BCZTSnx ($0.125 \leq x \leq 0.25$) ceramics.	141
6.2	Rietveld fitted X-ray diffraction pattern of BCZTSnx ($0.125 \leq x \leq 0.25$) ceramics via cubic phase having $Pm\bar{3}m$ space group.	142
6.3	Temperature-dependence of real (ϵ') and imaginary (ϵ'') part of dielectric permittivity for BCZTSnx ($0.125 \leq x \leq 0.25$) ceramics at 30 kHz.	144

6.4	The linear fitting of $\ln\left(\frac{1}{\epsilon} - \frac{1}{\epsilon_m}\right)$ vs. $\ln(T-T_m)$ plot for BCZTSnx ($0.125 \leq x \leq 0.25$) ceramics at 30 kHz.	146
6.5	The variation of $\frac{\partial \epsilon'(T)}{\partial T}$ vs. temperature (T) for BCZTSnx ($0.125 \leq x \leq 0.25$) ceramics at 30 kHz.	148
6.6	Room temperature Raman spectra of BCZTSnx ($0.125 \leq x \leq 0.25$) ceramics.	150
6.7	The peak fitting of the Raman spectra for BCZTSnx ($0.125 \leq x \leq 0.25$) ceramics.	151
6.8	Variation in peak width corresponding to 512 cm^{-1} (black dots), and 747 cm^{-1} (red dots) mode for BCZTSnx ($0.125 \leq x \leq 0.25$) ceramics.	152

List of tables

3.1	Lattice parameters and various agreement factors obtained from Rietveld refinements of room temperature X-ray diffraction data of BCSZT x ($0 \leq x \leq 0.20$) ceramics for cubic ($Pm\bar{3}m$) phase.	67
4.1	Structural parameters and various agreement factors obtained from the Rietveld refinements of the temperature-dependent X-ray diffraction patterns for BCSZT15.	87
4.2	Structural parameters and various agreement factors obtained from the Rietveld refinements of the temperature-dependent X-ray diffraction patterns for BCSZT15.	88
5.1	Factor group analysis of phonons in BaTiO $_3$	104
5.2	Structural parameters and various agreement factors obtained from the Rietveld refinements of the X-ray diffraction patterns for $x = 0$ via single-phase ($P4mm$) model.	110
5.3	Structural parameters, phase fraction, and various agreement factors obtained from the Rietveld refinements of the X-ray diffraction patterns for $x = 0.025$ via three-phase ($P4mm + Amm2 + R3m$) coexistence model. . . .	113

5.4	Structural parameters, phase fraction, and various agreement factors obtained from the Rietveld refinements of the X-ray diffraction patterns for $x = 0.05$ via two-phase ($Amm2 + R3m$) coexistence model.	114
5.5	Structural parameters and various agreement factors obtained from the Rietveld refinements of the X-ray diffraction patterns for $x = 0.075$ via single-phase ($R3m$) model.	114
5.6	Structural parameters, phase fraction, and various agreement factors obtained from the Rietveld refinements of the X-ray diffraction patterns for $x = 0.10$ via two-phase ($Pm\bar{3}m + R3m$) coexistence model.	116
5.7	Composition-dependent variations of Ti-O bond lengths (in Å) for BCZTS $_x$ ($0 \leq x \leq 0.10$) ceramics.	117
5.8	Amplitude of the phonon mode(s) in low symmetry ferroelectric phases of BCZTS $_x$ ceramics, with respect to high symmetry cubic ($Pm\bar{3}m$) phase. .	123
6.1	Structural parameters and various agreement factors obtained from Rietveld refinements of room temperature X-ray diffraction data of BCZTS $_x$ ($0.125 \leq x \leq 0.25$) ceramics via cubic ($Pm\bar{3}m$) phase.	143